THESIS

VOLUMETRIC CREATION OF ULTRA-HIGH-ENERGY-DENSITY PLASMA BY IRRADIATION OF ORDERED NANOWIRE ARRAYS

Submitted by

Clayton Bargsten

Department of Electrical and Computer Engineering

In partial fulfillment of the requirements

For the Degree of Master of Science

Colorado State University

Fort Collins, Colorado

Spring 2016

Master's Committee:

Advisor: Jorge J. Rocca

Mario C. Marconi
Jacob L. Roberts

ABSTRACT

VOLUMETRIC CREATION OF ULTRA-HIGH-ENERGY-DENSITY PLASMA BY IRRADIATION OF ORDERED NANOWIRE ARRAYS

Creating appreciable volumes of Ultra-High-Energy Density (UHED) matter in the laboratory is a challenge. Recent developments in the fabrication of vertically aligned nanowire array targets, in coordination with ultra-high-contrast femtosecond laser pulses focused to relativistic intensity, have opened the door to creating UHED matter using compact laser facilities with laser pulses of ~ 0.6 J. These high aspect ratio, vertically aligned nanostructure targets allow the laser energy to penetrate deep into the near-solid density material and heat plasmas to keV temperatures, generating Gbar pressures that are only surpassed in the laboratory by the central hot-spot of highly compressed thermonuclear fusion plasmas. The depth of the heated volume is key in governing the properties of these new UHED plasmas, and is reported here for the first time in vertically aligned nanowire arrays using a buried-tracer technique. In this study, arrays of 55 nm diameter nanowires, manufactured with a variable length segment of nickel on top of a buried cobalt segment, were irradiated with relativistic femtosecond laser pulses of $(4\pm1) \times 10^{19}$ W cm^{-2} intensity. Buried Co atoms are observed to ionize to the He-like state for depths greater than 4 µm, in good agreement with particle-in-cell simulations. The measured heat penetration demonstrates that the UHED plasma regime can be accessed with small high repetition rate lasers.

ACKNOWLEDGEMENTS

I am most grateful to have this opportunity to thank the many people who have helped and enabled me throughout my studies. First and foremost, I am thankful for the guidance of my advisor, Jorge Rocca, and hope to be as good a leader throughout my own career. Professors Carmen Menoni and Amy Prieto gave me unstintingly of their time not only in the classroom, but in the lab as well. The support and encouragement I received from Mario Marconi and Jacob Roberts is deeply appreciated.

I am particularly indebted to Reed Hollinger for working so closely with me on all our projects as we spent countless nights and weekends conducting experiments. I would like to acknowledge Michael Purvis and Duncan Ryan for setting up much of the infrastructure used in this project, and for the training they offered as I started my graduate work. Yong Wang, Shoujun Wang, and Alex Rockwood were indispensable in operating the laser. I am grateful for the insights gleaned through conversations with colleagues Brendan Regan and Alden Curtis. The nanowire targets were crucial to this work, and I wish to thank Everett Jackson, David Keiss, and Amanda Townsend for their assistance in making them. Vyacheslav Shlyaptsev and Alexander Pukhov were instrumental in the process of understanding experimental results through modeling and simulation. For experiments on the Titan Laser at Lawrence Livermore National Laboratory, I am glad to have worked with such a great team led by Riccardo Tommanssini, with colleagues Jaebum Park and Scott Andrews.

I am very thankful for my family and friends, in particular my parents and Junzhen (Annie) Zhang, who support and encourage me throughout every situation.

TABLE OF CONTENTS

LIST OF FIGURES

CHAPTER 1: INTRODUCTION

Section 1.1 Plasma Regimes

Plasma is the fourth state of matter and the most common form found in the visible universe. It is the fourth state because, with the addition of sufficient energy, it is the final state of all matter. Adding energy to a solid will eventually turn it into a liquid, then a gas, and finally a plasma. Plasmas are distinct from gases because they contain charged particles created by processes that allow electrons to leave their atoms. When this process of ionization results in a significant portion of the atoms being ionized, with proportional numbers of positive ions and unbound electrons present to leave the system macroscopically electrically neutral, we say that the matter has reached its plasma phase or state [1]. A part of what makes plasmas so interesting is that they can occur over a wider range of temperatures and densities than any other state of matter, from a low density of just a few ionized hydrogen atoms per cubic meter in interstellar space, to extreme densities in the center of stars. Common forms of plasmas in everyday life include the glow discharges found in certain lightbulbs, the lightening seen during a thunderstorm, and flames from fire. There is something to learn from every type of plasma, and new applications are constantly being developed.

Focusing on high-energy-density plasma, there are three comonly defined regions of interest, Warm Dense Matter, Hot Dense Matter, and Ultra-Hot Dense Matter. Each region is shown in Figure 1 with examples of some commonly associated forms of plasma. Warm dense matter is said to lie at the boundary between condensed matter and plasma physics because it is mostly degenerate and strongly coupled, with the kinetic energy of electrons typically comparable to the potential energy of their interactions with nuclei [2]. The conditions found in planetary

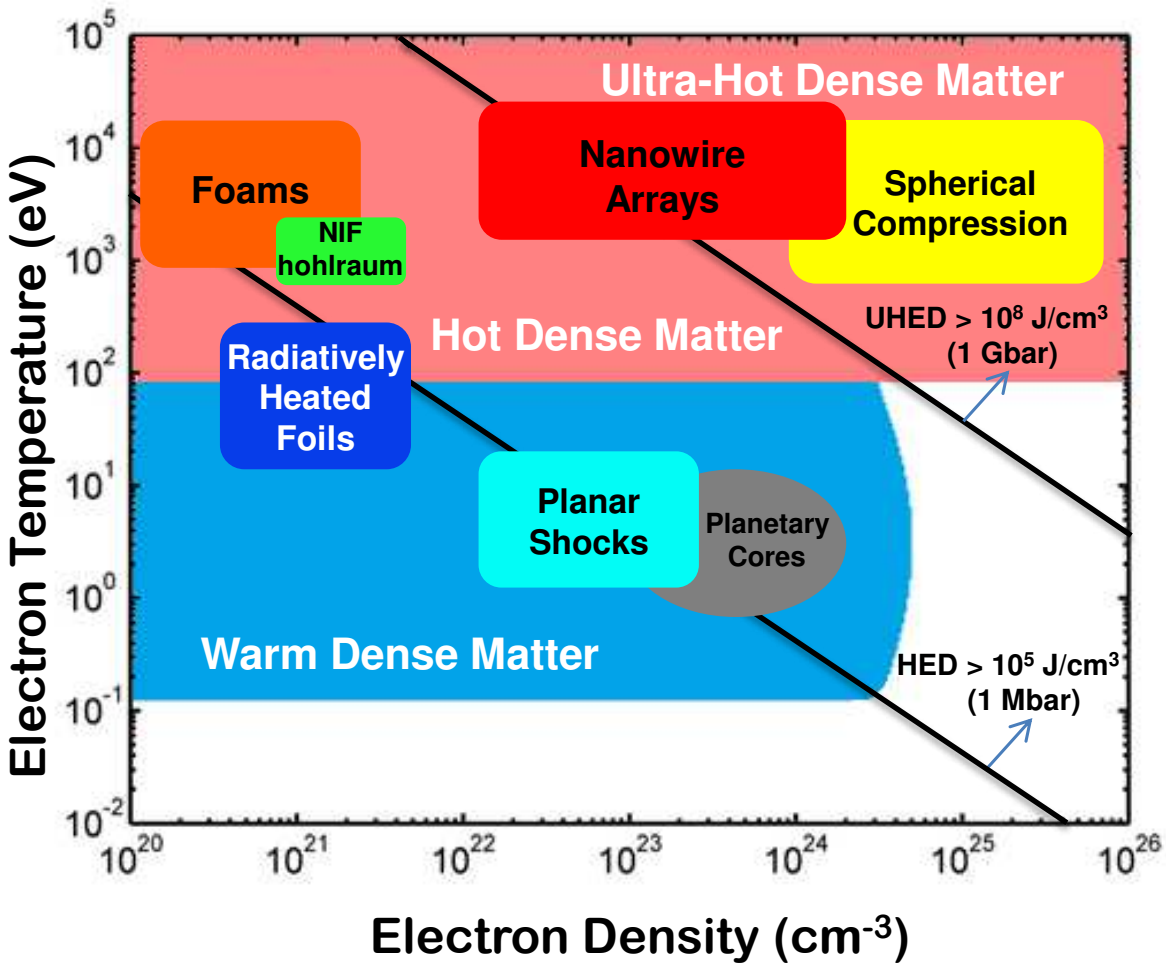

Figure 1: Parameter space showing high energy density matter regions of interest along with different forms of plasmas found in each regime. The plasma regimes accessible by irradiation of nanowires are compared with those of other HED and UHED plasmas. [Fig. ref. 7]

cores and planar shocks are prime examples of warm dense matter, with densities ranging up to 10 time that of solid density, and temperatures between 0.1 and 100 eV [3]. If the energy density rises further, the matter moves into the Hot Dense Matter regime, broadly characterized by temperatures greater than 100 eV and density greater than 0.1% of solid. More specific definitions are used in this regime, including both the High Energy Density (HED) and Ultra-High Energy Density (UHED) sub-regimes. HED matter is defined by matter with an energy density greater than 1 x 10^5 J cm^{-3}, corresponding to pressures in excess of 1 Mbar. Although planetary cores and

planar shocks can reach into this regime as well, it is dominated in the laboratory by laser-produced plasmas from foams or foils, self-pinching discharges, or targets heated by high energy particle beams [4]. At an energy density of 1 x 10^8 J cm^{-3}, or pressures greater than 1 Gbar, the UHED regime is reached. While UHED matter is found primarily in astrophysical bodies, it has been created in the laboratory at the center of spherical compression experiments [5,6]. It is also known in the present work that this regime can be generated with compact lasers [7].

Section 1.2 Laser-Produced High Energy Density Plasma

The process of answering many of today's important questions related to astrophysical [8, 9] and nuclear fusion phenomena [8, 10] can greatly benefit from study through laboratory access to sources of ultra-high-energy-density (UHED) plasma. Such matter can be, for example, a great source for high energy particles [11-13] and equation of state studies [14, 15]. Yet creating this extreme state of matter, defined by energy densities greater than 1 x 10^8 J cm^{-3} and corresponding to pressures in excess of 1 Gbar, is a major challenge. It requires adding energy to a system faster than it can cool through hydrodynamic expansion and radiation. The development of high power lasers has created an ideal method to quickly deposit large amounts of energy into a material. Figure 2a and 2b compare the energy density obtained from lasers with a variety of pulse lengths and energies respectively. To date, the irradiation of nanowire arrays as investigated in this thesis is the only source of laboratory UHED matter known to the author besides that created in the central hot spot of spherical compression experiments requiring use of the world's most powerful lasers [5, 6].

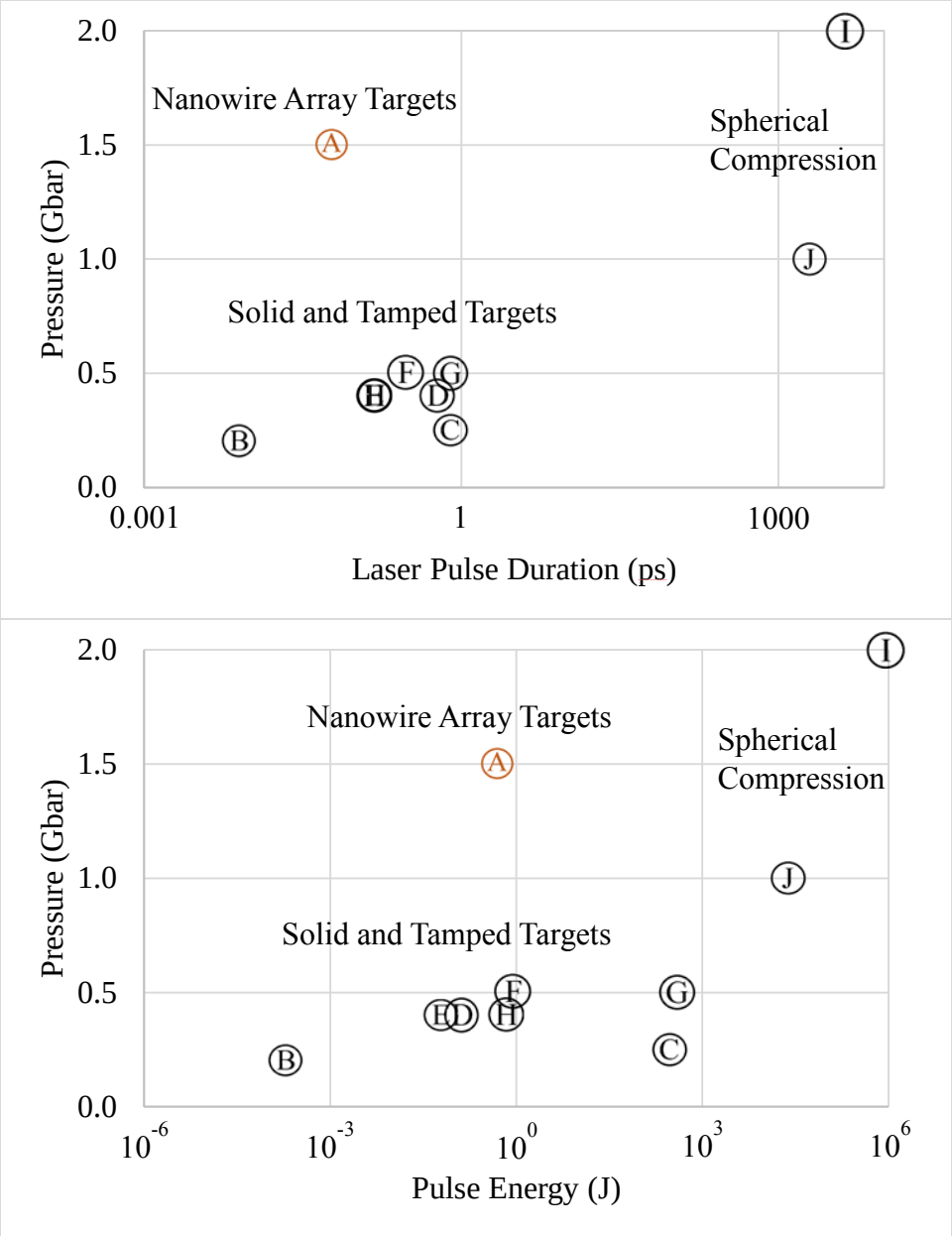

A) M. A. Purvis et al,. Nat. Photonics 7, 796–800 (2013).
B) J. Osterholz et al., Phys. Rev. Lett. 96, 085002 (2006).
C) R. G. Evans, et al., Appl. Phys. Lett. 86, 1 (2005).
D) A. Zigler, et al., Appl. Phys. Lett. 59, 534 (1991).
E) K. Eidmann, et al., J. Quant. Spectrosc. Radiat. Transf. 81, 133 (2003).
F) Z. Jiang, et al., Phys. Plasmas. 2, 1702 (1995).
G) K. U. Akli, et al., Phys. Rev. Lett. 100, 1 (2008).
H) A. Saemann, et al., Phys. Rev. Lett. 82, 4843 (1999).
I) S. Le Pape, et al., Phys. Rev. Lett. 112, 1 (2014).
J) R. Nora et al., Phys. Rev. Lett. 114, 045001 (2015).

Figure 2: The energy density of different laser-produced plasmas are compared against the pulse duration of the laser (top) and pulse energy (bottom). The types of targets used are also denoted along with the corresponding reference. One can see that nanowire targets offer significant opportunity for UHED creation using ultrafast lasers of modest scale that are more economically accessible than those of long pulse lasers.

The nanosecond pulses of these very high power lasers can heat material very efficiently and have produced large volumes of UHED plasma in the laboratory. Spherical compression geometries of targets are used with these lasers due to the long timescale of their pulses. Unless sufficiently confined by inertia or radiation pressure, the heated material will rapidly expand during the pulse interaction time. The spherical compression geometry requires very high pulse energies, and a high degree of experimental control over target and laser parameters including geometry, timing, and power [16]. For these reasons, such facilities are not yet economically available for wide-spread use.

Because of the complexity, scale, low repetition rate, and cost associated with these high-energy long-pulse lasers, ultrafast lasers can provide an alternate avenue to pursue the production of UHED matter with lower energy requirements. Using chirped-pulse-amplification techniques, lasers with sufficient bandwidth, such as Titanium:Sapphire lasers, can achieve femtosecond pulse durations [17]. This is the natural time-scale of the plasma volume's hydrodynamic expansion due to its speed of sound and physical dimensions [18]. However, ultrafast pulses have their own unique challenges when applied to the creation of UHED matter.

The simplest targets shot with ultrafast laser pulses are polished flat solid targets or planar foils, offering consistency between shots and ease of manufacture. When shot with an ultrashort laser pulse, they are quickly heated by the leading edge of the laser pulse causing plasma formation. An electromagnetic (EM) wave in plasma is governed by its dispersion relation given by,

$$\omega^2 = \omega_{pe}^2 + k^2 c^2,$$

where ω is the angular frequency of the laser light, ω_{pe} is the plasma frequency, and k is the wave-vector. One can quickly see that if $\omega < \omega_{pe}$ then the EM wave k-vector becomes imaginary and the wave is attenuated. This attenuation thus limits the depth to which the laser light can penetrate

a plasma and deposit its energy. Light penetration is limited by the plasma density where $\omega = \omega_{pe}$, which has a corresponding critical electron density defined as

$$n_c[cm^{-3}] = \frac{4\pi^2 \varepsilon_0 m_e c^2}{e^2 \lambda^2 10^6} \cong \frac{1.1\times10^{21}}{\lambda[\mu m]^2},$$

with permittivity of free space ε_0, electron mass m_e, speed of light c, and laser wavelength λ. Due to the quick formation of this critical electron density layer as the plasma expands away from the solid's surface, most of the subsequent light will be reflected and its energy prevented from penetrating into the dense material. In this way, the optical energy is inefficiently deposited into the high density layer above the critical region [19] and falls short of heating into the UHED regime.

Adding a top layer of different material to tamp the solid targets can help to reduce the rate of plasma expansion. By utilizing a low Z tamping material, the laser energy can heat a volume of material on the order of an optical skin-depth deep [20]. The heated electrons can then penetrate into the material and heat the material while its expansion rate is reduced [20, 21]. The added advantage of this setup is that the tamping material thickness can be varied and the experiment acts as one with a buried tracer layer. From the buried layer's spectroscopic data, the plasma's temperature and density can be characterized, and the depth of the heated volume determined. Because the depth of the heated volume will be on the order of the electron's mean-free path, the heated volume can range from a couple hundred nanometers in solid carbon and metals [20, 21] to tens of micron in light hydrocarbons [22]. Energy deposition at the critical layer and in the tamping material can prevent even this far denser layer from reaching UHED conditions.

If the laser pulse duration is shortened even further to the point where the total plasma expansion is negligible during the pulse, it is possible to make the evanescent field in the optical skin-depth the dominant heating mechanism. This requires pulses under 10 fs in duration, and leads to the laser's optical energy tunneling into the solid region of the target [19]. This method

again has limitations. The bandwidth required to produce such short pulses is large, making it difficult to amplify the pulses to large energies. At present, the generation of such short pulses is limited to low energy, and only a fraction of this energy will penetrate into the material [19]. Furthermore, while the energy is deposited at nearly solid-density, the skin-depth is very shallow and the heated layer is thus thin as well.

Novel target design offers an opportunity to attempt to overcome the absorption and penetration challenges. Nanostructures will generally offer a local field enhancement at the surface and increased levels of absorption [23]. However, only structures with large aspect ratios that provide vacant gaps in the solid material offer significant opportunity for the penetration of optical energy past the leading surface of the material and prevent the creation of a continuous critical electron density layer during the pulse interaction time. Of the nanostructures investigated to date in the literature (see Figure 3) gratings [24, 25] and 'smoked' or nanoparticle "cluster" coated surfaces [25, 26] offer absorption enhancements, but limited help with energy penetration into the material. Nanoporous membranes [27, 28] and nanowires [7, 29, 30], on the other hand, can be made with aspect ratios greater than 500 with appropriate amounts of space between structures for enhanced penetration of optical energy past the leading surface and allowing for volumetric heating of the material. Nanowire and nanoporous targets can thus drastically enhance both absorption and penetration mechanisms.

An added requirement of using nanostructured targets, however, is the need to avoid any significant pre-pulse before the arrival of the main laser pulse. Any preformed plasma will destroy the nanostructures, creating a continuous critical electron density layer, and negate the effects of using the structured surface. For this reason, laser pulses of ultra-high contrast are required when using nanostructured targets.

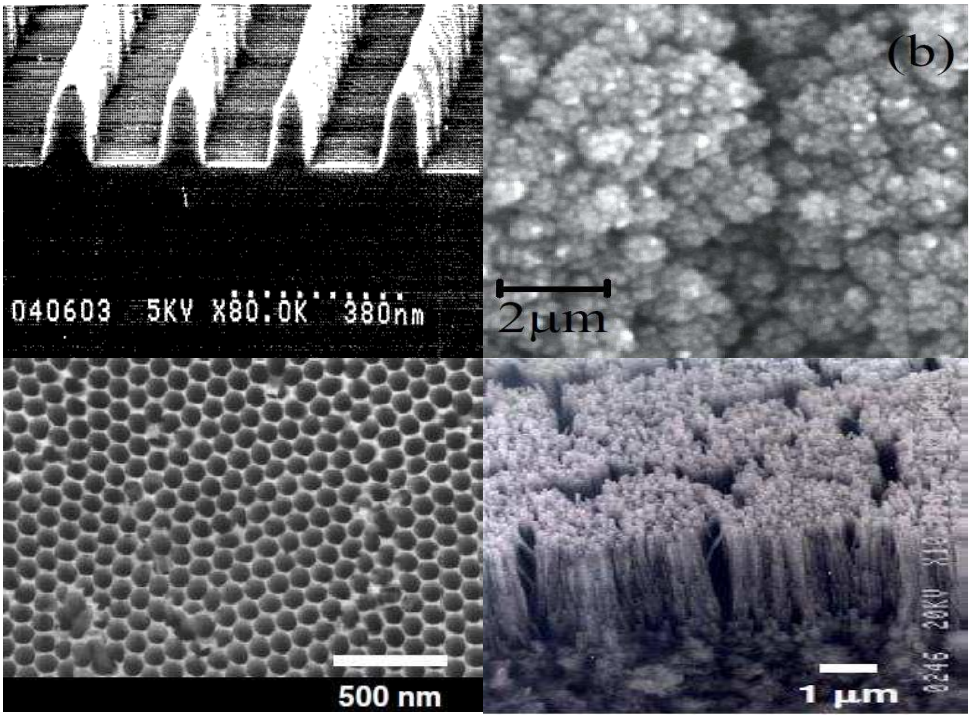

Figure 3: Different types of nanostructured surfaces used as targets for LPP experiments to create HED matter. Displayed nanostructures include gratings on the top-left [Fig. ref. 25], 'smoked' or clusters on the top-right [Fig. ref. 26], nanopores on the bottom-left [Fig. ref. 28], and nanowires on the bottom-right [Fig. ref. 29].

Section 1.3 Previous Work with Nanowire Targets and the Creation of UHED Plasma

Nanowires and nanowire arrays have become quite common, with a wide variety of applications including optoelectronics and sensors, solar cells, batteries, and lasers [31]. It is specifically the vertically aligned nature of the arrays with large aspect ratios and high density that makes them excellent targets for the creation of UHED. Figure 4 shows representative nickel nanowire arrays from this project with an average density corresponding to 13% and 30% of solid. The photo insert in Figure 4 also shows the strong absorption characteristic across the visible spectrum of these vertically aligned nanowire arrays as seen by eye.

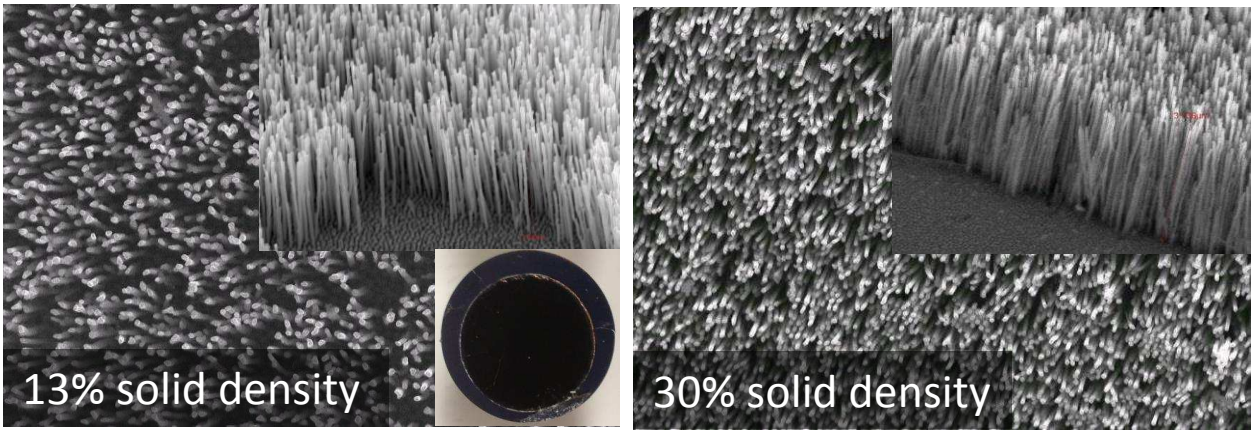

Figure 4: SEM images of vertically aligned nickel nanowire arrays. Arrays can be grown with densities ranging from 7% - 35% of solid density. The SEM profile view insets demonstrate their vertical and high aspect ratio properties. The photograph inset shows that the arrays exhibit strong absorption across the visible spectrum, even at low intensities seen by eye.

The combination of high material density in a form that strongly enhances absorption and allows for deep penetration makes vertically aligned, metallic nanowire arrays excellent targets to investigate volumetric heating of UHED plasmas by irradiation with ultra-high contrast, ultrafast laser pulses of relativistic intensity. In previous work, we have recently demonstrated the creation of UHED matter by irradiation of arrays of nickel nanowires with femtosecond pulses with an intensity of 5×10^{18} W cm^{-2} [7]. High degrees of ionization were observed from the plasmas, with nickel arrays ionized 26 times to the He-like state and gold ionized up to its Co-like state, Au^{+52}. What is also significant about the nanowire spectra (plotted in red in Figure 5) is that it shows a large difference in x-ray emission when compared to plasmas from polished flat targets (plotted in blue in Figure 5) irradiated under the same conditions. The continuum x-ray flux in the 1.5 – 1.75 Å (roughly 7 -8 keV) spectral region from the nanowire plasma exhibits over 50 times the x-ray yield of the flat target. The spectrum is dominated by the nickel He-like line 2p - 1s ($\lambda = 1.588$ Å) and intercombinatory lines of He-like Ni merged with Li-like Ni (surrounding $\lambda = 1.6$ Å). The He-like lines strongly dominate the K-α line ($\lambda = 1.658$ Å). This shows the importance of the

large density of energetic electrons in the bulk of the distribution that are required to generate the highly ionized species, whereas the K-α emission is instead produced primarily by high energy or "hot" electrons in the tail of the distribution interacting with neutral atoms.

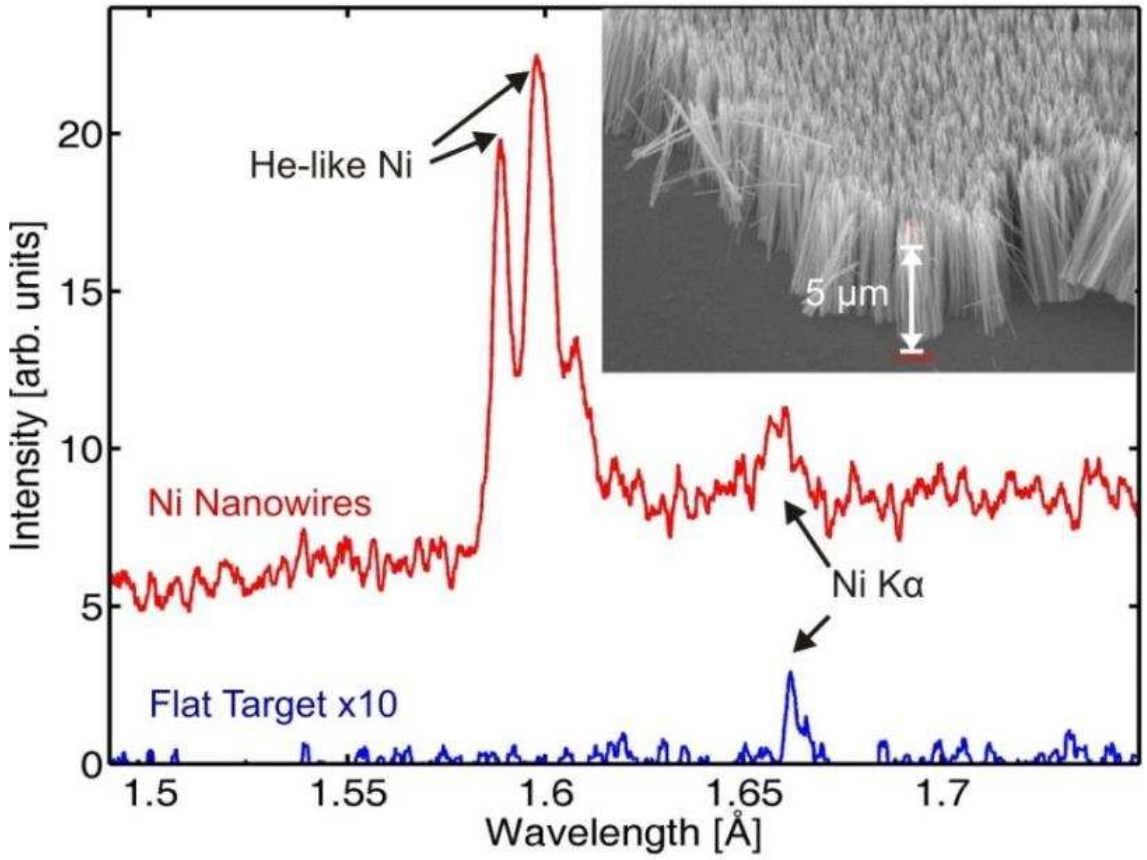

Figure 5: Spectra from the irradiation of nanowire (red) and solid flat targets (blue). The nanowire array consisted of 55 nm diameter nickel wires, 5 micron in length, with an array density of 13% of solid, and is shown in the SEM image insert. Both targets were irradiated at an intensity of 5 x 10^{18} W cm^{-2}. Signal from the flat target is shown in a scale that has been multiplied by a factor of 10. [Fig. ref. 7]

Models and simulations of the plasma parameters created using spectra from the nickel nanowire plasma suggest thermalized electron temperatures of 2 - 4 keV and densities of 3 x 10^{23} cm^{-3}, resulting in pressures surpassing a Gbar. Characterization of the penetration depth is

important to the validation of these calculations because it is a critical parameter governing the plasma properties. An initial measurement examined the relative intensity of the nickel He-α lines as a function of nanowire length to determine the length at which the signal saturates. The series of spectra in Figure 6 from that initial measurement correspond to different nanowire lengths and provide data that can be interpreted to suggest that a plasma with a depth of at least 3 - 4 µm was volumetrically heated to UHED conditions. However, the line radiation emitted by He-like ions below the surface may be absorbed by other ions over the plasma's depth before escaping from the plasma. The opacity of this single composition plasma thus adds a degree of uncertainty in interpreting the results, preventing a definitive measurement of the maximum heat penetration depth. For this reason, a two-composition buried tracer technique was developed as the focus of this thesis in order to better determine the penetration of energy in vertically aligned nanowire array targets. The buried-tracer study and results obtained are discussed in the following chapters.

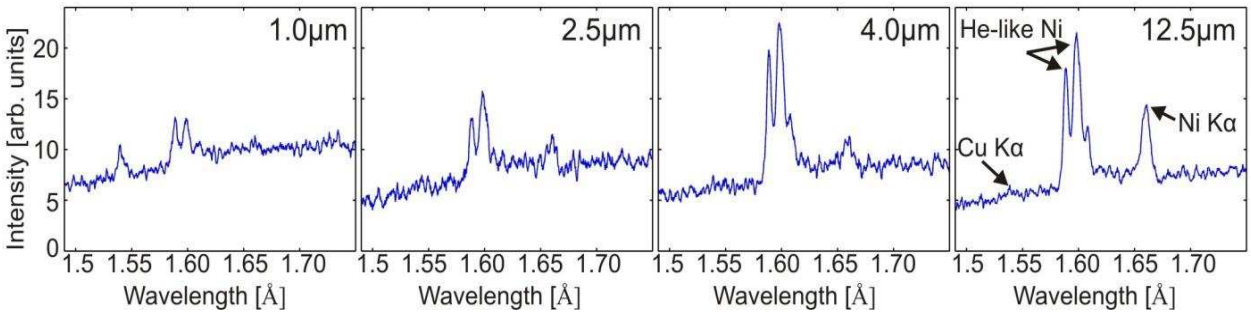

Figure 6: Original measurement suggestive of the heat penetration depth in nickel nanowire plasma. The wires that compose the target array are 55 nm in diameter with an atom density 13% of solid, irradiated at 5 x 10^{18} W cm^{-2}. Intensity of the nickel He-like lines is monitored as a function of the wire length and shown to saturate for wires over 4 micron in depth while the K-α continues to grow. This measurement is deemed inconclusive due to opacity effects in the plasma. [Fig. ref. 7]

REFERENCES

1. F. F. Chen, *Introduction to Plasma Physics and Controlled Fusion, Volume 1: Plasma Physics* (Springer US, 2nd ed., 1984), pp. 1–4.
2. Li et al., *Probing the warm dense copper nano-foil with ultrafast electron shadow imaging and deflectometry*. High Energy Density Phys. 8, 298–302 (2012).
3. M. Koenig et al., *Progress in the study of warm dense matter*. Plasma Phys. Control. Fusion. 47, B441–B449 (2005).
4. R. M. More, K. H. Warren, D. a. Young, G. B. Zimmerman, *A new quotidian equation of state (QEOS) for hot dense matter*. Phys. Fluids. 31, 3059 (1988).
5. R. Nora et al., *Gigabar Spherical Shock Generation on the OMEGA Laser*. Phys. Rev. Lett. 114, 045001 (2015).
6. S. Le Pape et al., *Observation of a reflected shock in an indirectly driven spherical implosion at the National Ignition Facility*. Phys. Rev. Lett. 112, 1–5 (2014).
7. M. A. Purvis et al., *Relativistic plasma nanophotonics for ultrahigh energy density physics*. Nat. Photonics. 7, 796–800 (2013).
8. E. I. Moses et al., *The National Ignition Facility: Ushering in a new age for high energy density science*. Phys. Plasmas. 16, 041006 (2009).
9. B. A. Remington, *High energy density laboratory astrophysics. Plasma Phys. Control. Fusion*. 47, 191 (2005).
10. E. I. Moses, *Advances in inertial confinement fusion at the National Ignition Facility (NIF)*. Fusion Eng. Des. 85, 983 (2010).
11. J. Workman et al., *Development of intense point x-ray sources for backlighting high energy density experiments (invited)*. Rev. Sci. Instrum. 75, 3915 (2004).
12. Y. Sentoku et al., *High-energy ion generation in interaction of short laser pulse with high-density plasma*. Appl. Phys. B Lasers Opt. 74, 207 (2002).
13. L. A. Bernstein et al., *Low Energy Neutron Measurements in High Energy Density Plasmas using the National Ignition Facility*. Plasma Fusion Res. Regul. Artic. X (2013).
14. B. K. Godwal et al., *Equation of State Theories of Condensed Matter Up To About 10 TPa*. Phys. Rep. 3, 121–197 (1983).
15. S. Ichimaru and H. Kitamura, *Pycnonuclear reactions in dense astrophysical and fusion plasmas*. Phys. Plasmas. 6, 2649 (1999).
16. J. Nuckolls, et al., *Laser Compression of Matter to Super-High Densities: Thermonuclear (CTR) Applications*. Nature. 239, 139–142 (1972).
17. D. E. Spence, et al., *60-fsec pulse generation from a self-mode-locked Ti:sapphire laser*. Opt. Lett. 16, 42–44 (1991).
18. R. P. Drake et al., *Observation of forward shocks and stagnated ejecta driven by high-energy-density plasma flow*. Phys. Rev. Lett. 81, 2068–2071 (1998).
19. J. Osterholz et al., *Production of Dense Plasmas with sub-10-fs Laser Pulses*. Phys. Rev. Lett. 96, 085002 (2006).
20. K. Eidmann et al., *K-shell spectra from hot dense aluminum layers buried in carbon and heated by ultrashort laser pulses*. J. Quant. Spectrosc. Radiat. Transf. 81, 133–146 (2003).

21. A. Saemann et al., *Isochoric Heating of Solid Aluminum by Ultrashort Laser Pulses Focused on a Tamped Target*. Phys. Rev. Lett. 82, 4843–4846 (1999).
22. R. G. Evans et al., *Rapid heating of solid density material by a petawatt laser*. Appl. Phys. Lett. 86, 1–3 (2005).
23. P. P. Rajeev, et al., *Nanostructures, local fields, and enhanced absorption in intense light-matter interaction*. Opt. Lett. 29, 2662–2664 (2004).
24. J. Gauthier et al., *Femtosecond laser-produced plasma x-rays from periodically modulated surface targets*. SPIE. 2523, 242–253.
25. M. M. Murnane et al., *Efficient coupling of high-intensity subpicosecond laser pulses into solids*. Appl. Phys. Lett. 62, 1068 (1993).
26. F. Y. Khattak et al., *Enhanced He-α emission from "smoked" Ti targets irradiated with 400 nm, 45 fs laser pulses*. EPL (Europhysics Lett. 72, 242 (2005).
27. S. P. Gordon, et al., *X rays from microstructured targets heated by femtosecond lasers*. Opt. Lett. 19, 484–486 (1994).
28. T. Nishikawa et al., *Nanohole-array size dependence of soft x-ray generation enhancement from femtosecond-laser-produced plasma*. J. Appl. Phys. 96, 7537–7543 (2004).
29. T. Nishikawa, et al., *Efficient water-window X-ray pulse generation from femtosecond-laser-produced plasma by using a carbon nanotube target*. Appl. Phys. B Lasers Opt. 78, 885–890 (2004).
30. G. Kulcsár, et al., *Intense Picosecond X-Ray Pulses from Laser Plasmas by Use of Nanostructured "Velvet" Targets*. Phys. Rev. Lett. 84, 5149 (2000).
31. L. Tsakalakos et al., *Strong broadband optical absorption in silicon nanowire films*. J. Nanophotonics. 1, 013552 (2007).

CHAPTER 2: EXPERIMENTAL SETUP

Section 2.1 Laser Setup

All experiments were conducted using the high power Ti:Sapphire laser at Colorado State University. The laser makes use of chirped-pulse amplification to amplify the output from a mode-locked Ti:Sapph oscillator through a chain of power amplifiers. The oscillator utilizes passive Kerr mode-locking to generate ~ 30 fs pulses centered at a wavelength of 800 nm. Pulses from the oscillator are stretched and then amplified in up to five stages of multi-pass amplification. To conduct the experiments discussed in the next chapter, pulses with ~ 2 J of energy were compressed using a grating compressor having an efficiency of ~ 65%. The pulse duration was measured using a second-harmonic generation frequency-resolved optical gate (SHG FROG) to be ~ 55 fs FWHM upon exiting the compressor. SHG FROG traces and reconstructions are shown in Figure 7.

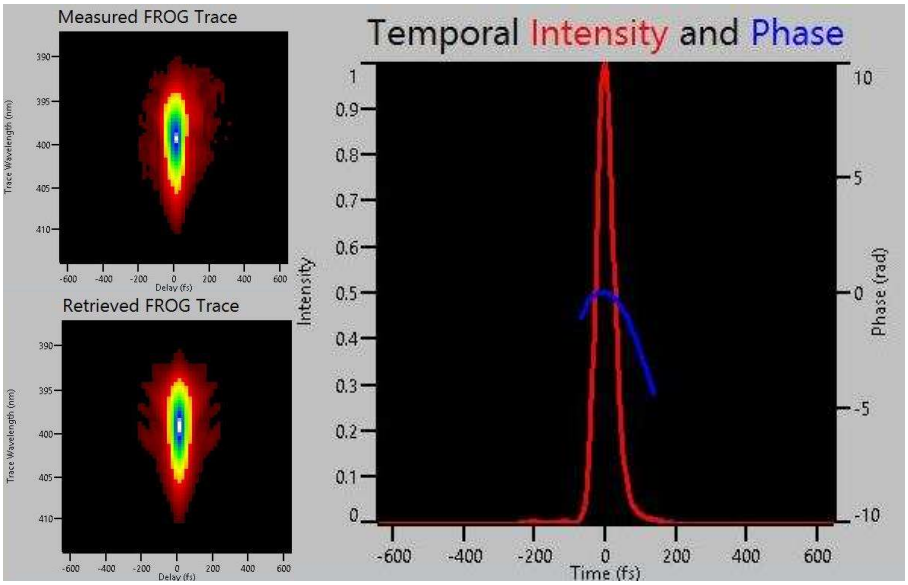

Figure 7: FROG traces and reconstructions showing the ~ 55 fs FWHM pulse duration.

Frequency doubling of the compressed pulses in a 0.8 mm thick Type I KDP crystal placed at the output of the compressor increases the pulse contrast in order to prevent damaging the nanowires prior to the arrival of the main pulse. Laser contrast at the fundamental frequency was measured on the picosecond scale with a 3rd-order scanning autocorrelator, and on the nanosecond scale with a filtered photodiode prior to each data run. The contrast at the fundamental frequency is measured to be greater than 5 x 10^6. A set of four highly selective dichroic mirrors after the doubling crystal separate the fundamental 1ω pulse from the doubled 2ω ($\lambda = 400\,nm$) light. The mirrors were designed to reflect 99.9% of the 2ω beam and transmit 98.5% of the 1ω beam giving a contrast of 2 x 10^7 between 2ω and 1ω pulses from the dichroic system, resulting in a total pre-pulse contrast greater than 1 x 10^{12} at 2ω. At an intensity of (4 ± 1) x 10^{19} W cm^{-2}, the pre-pulse is then reduced to an on target intensity below the damage threshold of the nanowires, and leaving the targets intact for the arrival of the main pulse.

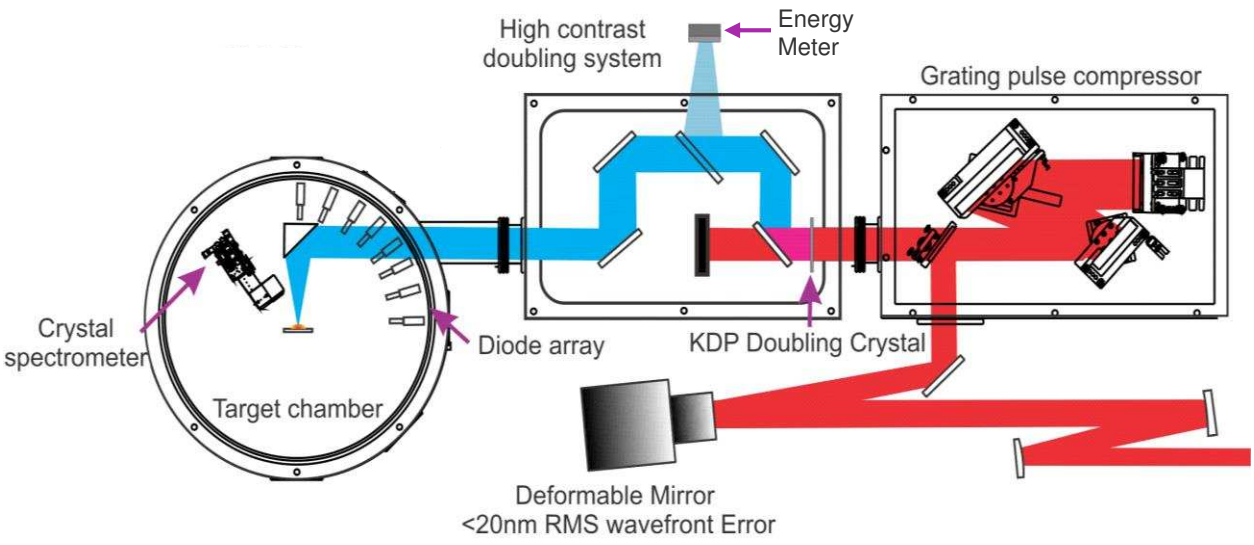

Figure 8: Experimental setup including the pulse compressor, dichroic mirror sequence, and target chamber.

A diagram of the experiment is shown in Figure 8. The final optic is an f/2.7, protected aluminum, 90 degree off-axis parabola for focusing the frequency doubled pulses onto the target. The spot focus size and shape are intimately tied to the distortions in the beam's wavefront, which is optimized by a Shack-Hartmann wavefront sensor fed back into a deformable mirror placed just prior to the entrance to the pulse compressor. A $1/e^2$ focal diameter of ~ 5 µm is achieved with this OAP, as measured by imaging onto a CCD with a 10X objective prior to each data run and shown in Figure 9. The total energy on target is ~ 0.6 J. Energy is measured on a shot-by-shot basis using a 500 µm thick beam splitter coated to divert 1% of the 2ω energy to a pyroelectric energy meter. The laser beam is focused onto the targets at normal incidence, achieving an intensity of $(4 \pm 1) \times 10^{19}$ W cm^{-2}. The spectrum of the x-ray radiation emitted by the plasma was observed by a von Hamos crystal spectrometer placed at ~ 45 degrees off normal.

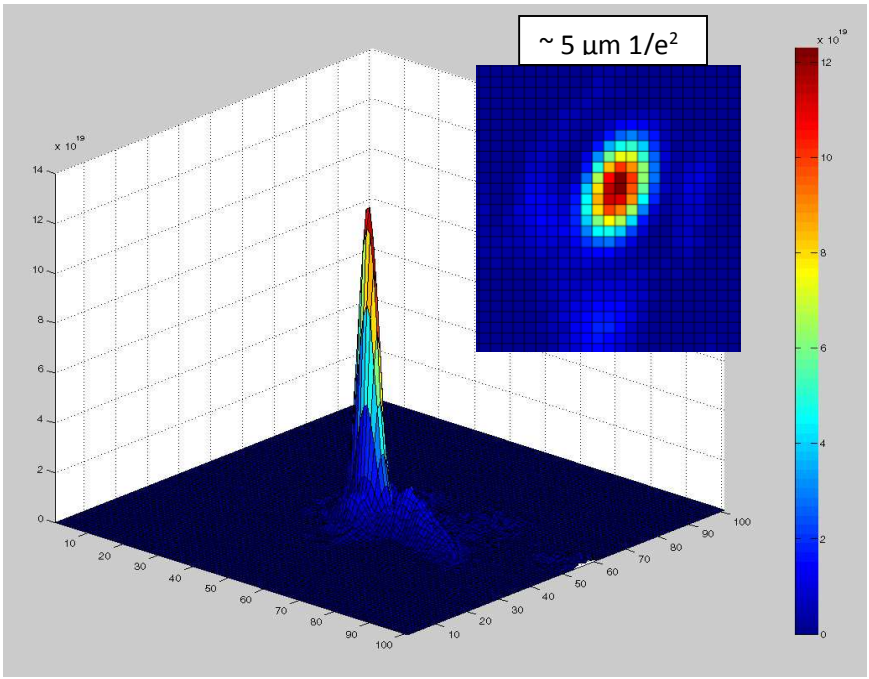

Figure 9: The spot focus achieved with the final OAP focusing optic and used during this experiement. The inset shows the spot shape while the larger 3D plot shows a contour mapping of the intensity across the focal spot.

Section 2.2 Vertically Aligned Nanowire Array Targets

Of the two primary high aspect-ratio targets of interest, nanopores and nanowires, the current advantage of nanowires lies in their ability to be manufactured from a far wider variety of materials than nanopores. Nanopores are currently limited to materials that display special nanoscale self-organization properties in the material under certain chemical and electrical potentials [1]. While the self-assembly property of nanopores is well known and characterized in anodization processes, the fact that the structures are made of oxides can be a limitation. While lithographic and FIB techniques may be able to produce the required porous or wire structures, the cost and effort of manufacture using these techniques is far higher than growing nanowires electrolytically as was done for this thesis. Using electrolytic techniques allows for the production of metallic nanowires from many mid to high-Z metals.

Template-assisted synthesis is a well-known "bottom-up" technique and was used to manufacture the arrays used in this project [2]. Anodic aluminum oxide (AAO) membranes are used as the templates for growing the arrays. As mentioned above, AAO demonstrates a self-organizing property on the nanoscale when the anodization process occurs in an acidic environment. With careful control over the pH, choice of acid, and anodization voltage, the pore diameter and density can be controlled [2]. As AAO templates are used commercially for a wide range of filtration and sensing applications, they are available from several vendors. While templates with pore diameters of 18 – 200 nm in diameter and porosities from 7 – 35% are available, the templates used to make arrays for this project had 55 nm diameter pores with a porosity (which becomes the array density) of 13%.

A general depiction of the vertically aligned nanowire array fabrication process can be seen in Figure 10. The process of synthesizing the nanowire array begins with the evaporation of a thin chromium wetting layer (~ 10 nm) followed by a gold layer (~ 750 nm thick) onto one side of the AAO template. This gold layer serves many purposes. It seals one end of the pores to become the base of the nanowire array while at the same time acting as an electrical contact for the electrodeposition of the wire material into the template's pores. Gold is chosen because of its excellent chemical stability with regards to the chemicals used in the deposition process. In this regard, the thin gold layer serves to buffer and protect all the other components from the eroding conditions of the deposition baths and subsequent dissolving of the template. The mechanical properties of gold also give the thin film low stress, and prevent it from breaking the fragile AAO membranes which are less than 50 µm thick.

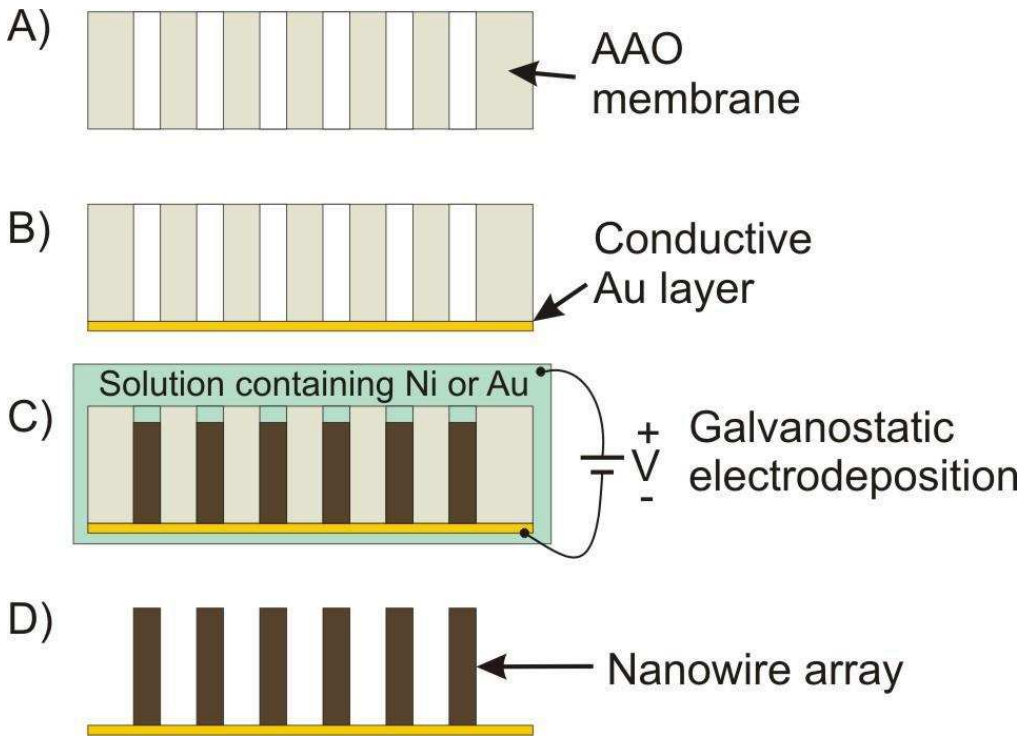

Figure 10: Process of synthesizing vertically aligned nanowire array. [Fig. ref. 3]

Gold backed templates are placed on SEM stubs with an electrically conductive copper tape in final preparation for the wire synthesis and deposition. A generic Watts Bath solution is used for the deposition of both nickel and cobalt materials. When a voltage is applied across the solution and gold electrode, the positive ions in solution will deposit at the base of the pores. This galvanostatic electrodeposition allows for the wires to be grown to a desired length inside the template pores. As the buried tracer experiment of this thesis required the wires to consist of two distinct layers or segments, cobalt was first deposited in the pores to a length of at least 3 µm, followed by subsequent deposition of nickel at a variable length from 1 – 6 µm. High resolution transmission electron microscope analysis of the junction revealed that the junction between the Co and Ni layers was smaller than 100 nm in length.

Once the deposition is complete, wires must be freed from the AAO template through a dissolving process in 4M NaOH. Throughout the deposition and dissolving process, the array never leaves solution. Surface tension in the liquid droplets will bunch the wires as they dry. It is thus necessary to dry the arrays in a supercritical CO_2 bath where the supercritical fluid can be released as a gas and completely skip any phase with wire damaging surface tension. This process allows for wires of very large aspect ratio (ratio > 200) to be made, yet remain well aligned vertically. This is key for the long wires of dual composition for the buried tracer experiment, as the wires must be long to accommodate the two required layers. An example of the large aspect-ratio, two-composition wire arrays, as imaged by energy dispersive x-ray spectroscopy (EDS), can be seen in Figure 11.

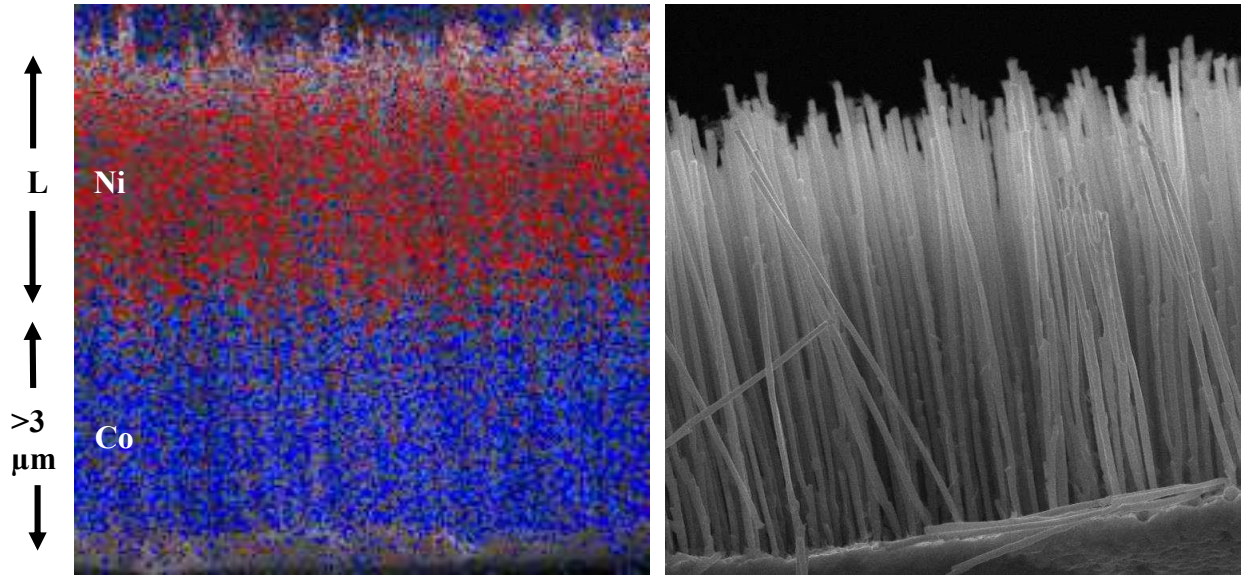

Figure 11: EDS image showing the Ni segment on top of the buried Co layer (left). The large aspect ratio of the wires is apparent in the SEM profile scan (right).

Section 2.3 von Hamos X-ray Crystal Spectrometer

The main diagnostic used for the measurements is a von Hamos x-ray crystal spectrometer. X-ray spectrometers are an important diagnostic tool used to characterize a laser-created plasma. With proper calibration and adequate resolution, it can reveal fine details regarding line emission and photon flux from continuum radiation over different regions of the electromagnetic spectrum. Line radiation can be used to identify the atomic composition and the degrees of ionization found in a plasma. Shifts and widths of atomic lines along with ratios between line intensities and continuum can be related to conditions in the plasma such as temperature and density [4].

Diagnosing the plasma in this project required an efficient, high resolution x-ray spectrometer. Crystals can naturally meet these requirements through constructive interference from Bragg Scattering off of successive lattice planes throughout the bulk of the crystal material. A diffractive element was needed to meet these needs over the 1.5 – 1.8 Å spectral region where

the characteristic line radiation of interest for nickel and cobalt atoms lies. While multiple crystals could possibly meet the requirements, the geometry of the spectrometer must also be considered for efficiency and resolution. For this project, a von Hamos spectrometer configuration was selected due to its simplicity and high efficiency for recording the emission of quasi-point sources [5]. The von Hamos geometry is illustrated in Figure 12. In the von Hamos configuration, a cylindrically bent crystal with radius R collects photons and focuses them onto its central axis, strongly enhancing the efficiency of the device. The distribution of the wavelengths along the axis are governed by the Bragg diffraction relation

$$n\lambda = 2d \sin\theta$$

where the diffraction order n, wavelength λ, and crystal lattice spacing d, define the scattered angle θ, and thus the location of the diffracted wavelength on the axis to be imaged by a CCD. The total distance from plasma source to image location on the cylindrical axis is found to be

$$Z = 2R\sqrt{\left(\frac{2d}{n\lambda}\right)^2 - 1}.$$

Accounting for crystal efficiency in the desired spectral region, the physical capabilities of the crystal material to be cylindrically bent, and given the space limitations in the experimental vacuum chamber, a mica crystal with 2d spacing of 19.84 Å and bending radius of 2 cm was used. This configuration requires the use of the crystal in its third order, and thus that the detector be placed at a distance Z of just over 16 cm. A small removable rod of the proper length, aligned with the imaging cylinder's axis allowed for accurate pointing of the von Hamos at the plasma, and ensured that it was placed at the proper distance. The spectra taken in this configuration were calibrated using the copper, nickel, and cobalt K-α lines. The instrument was found to have resolution better than 0.005 Å across the full spectral viewing window.

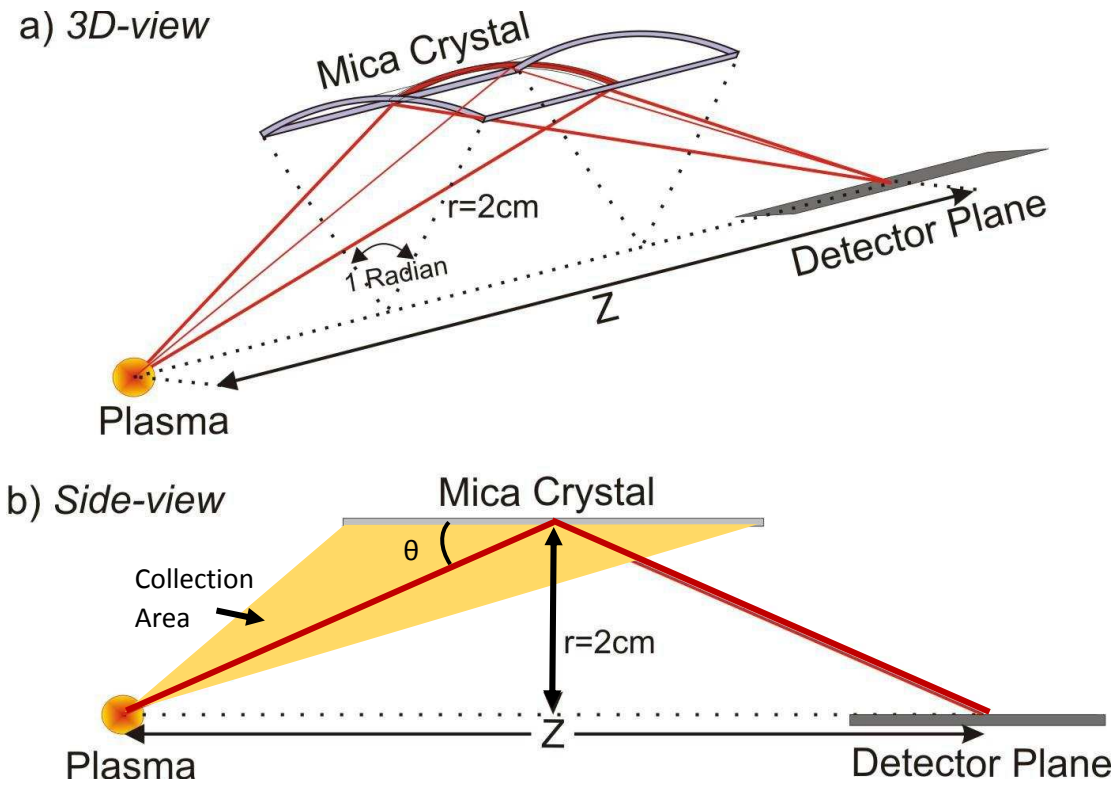

Figure 12: Schematic drawing of the von Hamos crystal spectrometer shown in a 3D view (a), and side view (b). Rays are collected by the cylindrically bent mica crystal with a radius of 2 cm and spanning 1 radian of the cylinder circumference. The crystal is 50 mm long and placed at the midpoint between the plasma and detector. The detector is situated at a distance Z of roughly 160 mm from the plasma and with its imaging surface along the cylinder axis so as to image the Ni and Co He-α radiation that is Bragg reflected from the crystal at an angle θ. [Fig. ref. 3]

Other design considerations in addition to the crystal material and geometry had to be met prior to building and using the spectrometer. A CAD drawing and image of the final von Hamos setup is found in Figure 13. An E2V 4240 2-dimensional array CCD detector was selected for its responsivity and 16-bit well depth, enabling it to have a large dynamic range for imaging the spectra collected by the mica crystal. The 2D nature of the sensor also allows for one to be certain that the CCD has been placed optimally in the focal plane of the crystal. Protecting the CCD from the plasma's EM noise required building an electrically sealed alodine coated housing for the CCD and readout electronics that could properly hold the CCD in the crystal's focal plane, yet still be

attached to a standard translation stage and moved with precision by picomotors. An electrically conductive, vacuum compatible grease was found that overcame the challenge of electrically sealing the exchangeable 12.5 µm thick Aluminum foil filter needed to cover the faraday box aperture that allowed the collected spectra to be imaged onto the CCD. In addition to preventing the entrance of visible light and cutting contributions from lower orders that would contaminate the desired 3rd-order signal, the Al filter was selected to prevent saturation of the most intense lines while still utilizing the maximum dynamic range of the CCD.

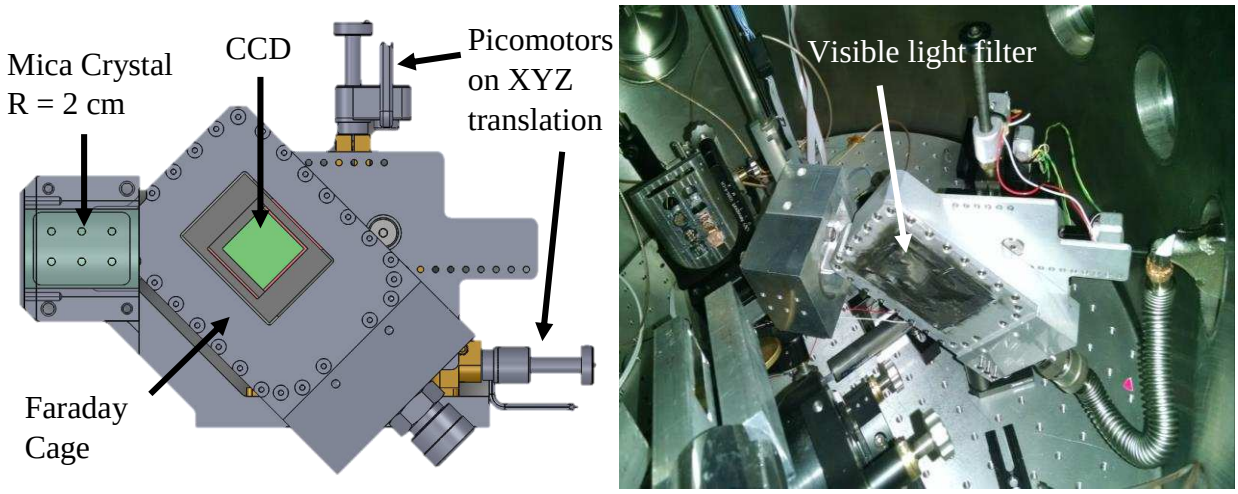

Figure 13: Schematic (left) and photograph (right) of the von Hamos crystal spectrometer used for collecting x-ray spectral data in the 1.5 – 1.8 Å region for this project.

The efficiency of the von Hamos spectrometer configuration was assessed as diagnostic instrument. First, the collection angle of the instrument must be considered. It is determined by the physical dimensions of the crystal and its placement at ~ 80 mm from the plasma, as required to meet the Bragg conditions for imaging Ni and Co He-α lines. The schematic in Figure 12 (b), illustrates all the relevant dimensions related to the collection solid angle of the crystal's viewing

window. The collection solid angle is roughly 0.0754 sr, corresponding to a collection efficiency of $\eta_{CE} \cong 0.012$ in the 2π hemisphere of emission. Of the x-ray light collected by the crystal, only a small percentage is reflected. The reflection efficiency depends on the crystal material, geometric configuration, and crystal order being used to diffract the desired wavelength region. Reflection efficiency for the cylindrically bent mica crystal with radius of 2 cm was taken from the work of Shevelko, with his plot reproduced in Figure 14. The values for a mosaic crystal (see dashed line) predict a reflection efficiency of $\eta_R \cong 9 \times 10^{-5}$ when the crystal is used in 3rd order for the Ni He-like lines [5].

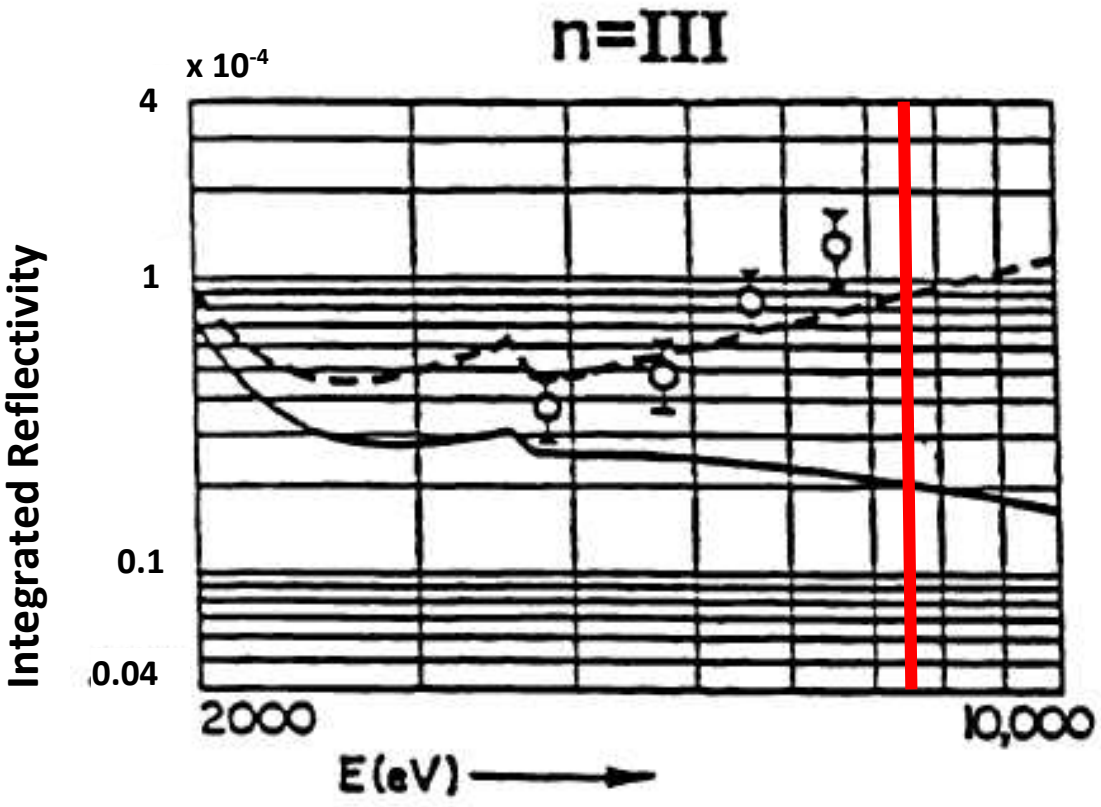

Figure 14: Integrated reflectivity values from cylindrically bent mica crystal with R = 2 cm and used in 3rd order. Experimental data points are compared with theoretical curves for a mosaic (dashed) and perfect (solid) crystal models. The region of interest to this project around the Co and Ni He-like lines is indicated in red. [Fig. ref. 5]

The collected light experiences further loss as it passes through a 12.5 μm thick Al filter used to block visible light and contributions from lower diffraction orders. When light passes through the filter at the Bragg angle of θ ~ 14°, the effective thickness of the Al filter becomes ~ 50 μm, and the filter's transmission efficiency is found to be $\eta_F \cong 0.46$. The same projection at the Bragg angle must be taken into account for the depth of the depletion region in the Si CCD detector. Due to the depletion region's finite thickness, only a fraction of the photons that make it to the CCD will actually be absorbed to create electron-hole pairs and contribute to the observed signal. The layer is nominally ~ 16 μm thick [6], giving a projected effective thickness of ~ 64 μm, and thus an absorption efficiency of $\eta_A = 1 - T \cong 0.66$. Accounting for all of these losses, the detector system efficiency is found to be $\eta_{syst} = \eta_{CE}\eta_R\eta_F\eta_A \cong 3.3 \times 10^{-7}$ relative to 2π emission.

From the detector efficiency and counts on the CCD, the plasma's photon emission in a given bandwidth can be estimated. A typical spectra might have ~ 10^7 counts in the nickel He-α line on the CCD. If each count corresponds to roughly 1.5 collected electron-hole pairs due to the electronic readout gain, G, and the quantum efficiency of the silicon detector is found as the ratio of the incident photon's energy to the 3.65 eV required to produce e-h pairs in the detector, $QE = hv/(3.65\ eV)$, then the plasma's emitted photon intensity can be estimated as

$$\dot{N}_{ph} = \frac{counts \cdot G}{QE \cdot BW \cdot 2\pi \cdot \eta_{syst}}$$

where BW is the bandwidth, and the emission is evaluated over a hemisphere of 2π sr. The bandwidth for the He-α line is ~ 0.006 Å, including instrumental broadening. Together, these values give an estimated plasma emission in the nickel He-α line of $\dot{N}_{ph} \approx 6 \times 10^{11} \frac{ph}{sr\ Å}$.

REFERENCES

1. F. Li, et al., *On the growth of highly ordered pores in anodized aluminum oxide*. Chem. Mater. 10, 2470–2480 (1998).
2. Y. Liang, et al., *Preparation of free-standing nanowire arrays on conductive substrates*. J. Am. Chem. Soc. 126, 16338–16339 (2004).
3. M. A. Purvis. PhD Dissertation. *Relativistic Plasma Nano-Photonics for Ultra-High Energy Density Physics*. 2014.
4. W. L. Wiese, et al, *Detailed Study of the Stark Broadening of Balmer Lines in a High-Density Plasma*. Phys. Rev. A. 6, 1132 (1972).
5. A. P. Shevelko, *X-ray spectroscopy of laser-produced plasmas using a von Hamos spectrograph*. Proc. SPIE Curr. Russ. Res. Opt. Photonics New Methods Instruments Space-Earth-based Spectrosc. XUV, UV, IR, Millim. Waves. 3406, 91–108 (1998).
6. P. R. Jorden, et al., *Secrets of E2V Technologies CCDs (Ex Marconi CCDs)*. Exp. Astron. 14, 69–75 (2002).

CHAPTER 3: PENETRATION DEPTH RESULTS AND CONCLUSIONS

Section 3.1 Heat Penetration in Vertically Aligned Nanowire Array Plasmas

When a nanowire array is irradiated by an ultra-high contrast laser pulse of relativistic intensity, the depth to which its energy can penetrate is a key parameter in understanding the created plasma. Knowledge of the penetration depth allows for the determination of the initial volume and energy density of the plasma. The method for determining the depth of the heated volume for this project was to use targets with a layer of different material buried at variable depths from the target's surface. This material produces a spectroscopically distinct signal when heated appropriately. The relative intensity of that signal can be related to depth at which the layer is buried, and thus the depth to which heat is penetrating in the target.

Several important factors were considered when selecting the materials used in the layers in the nanowire arrays of this experiment. It has already been discussed that the arrays were manufactured with the bottom segment of each wire made of cobalt, while the top segment was made of a variable length of nickel, illustrated in Figure 15 (a, b). Nickel and cobalt were chosen due to their good mechanical properties, producing arrays of high quality and order. Their similar electrochemical properties allow them to be manufactured using the same equipment as well. Due to the fact that they are nearest neighbors on the periodic table, their k-shell emission is sufficiently close in energy to be imaged within the same window of a single crystal spectrometer as is shown in Figure 15 (c). Most importantly, cobalt's line radiation is shifted enough relative to that of nickel to negate the opacity effects due to resonant absorption of a single composition plasma that obscured definitive assessment of penetration depth in the first experiment.

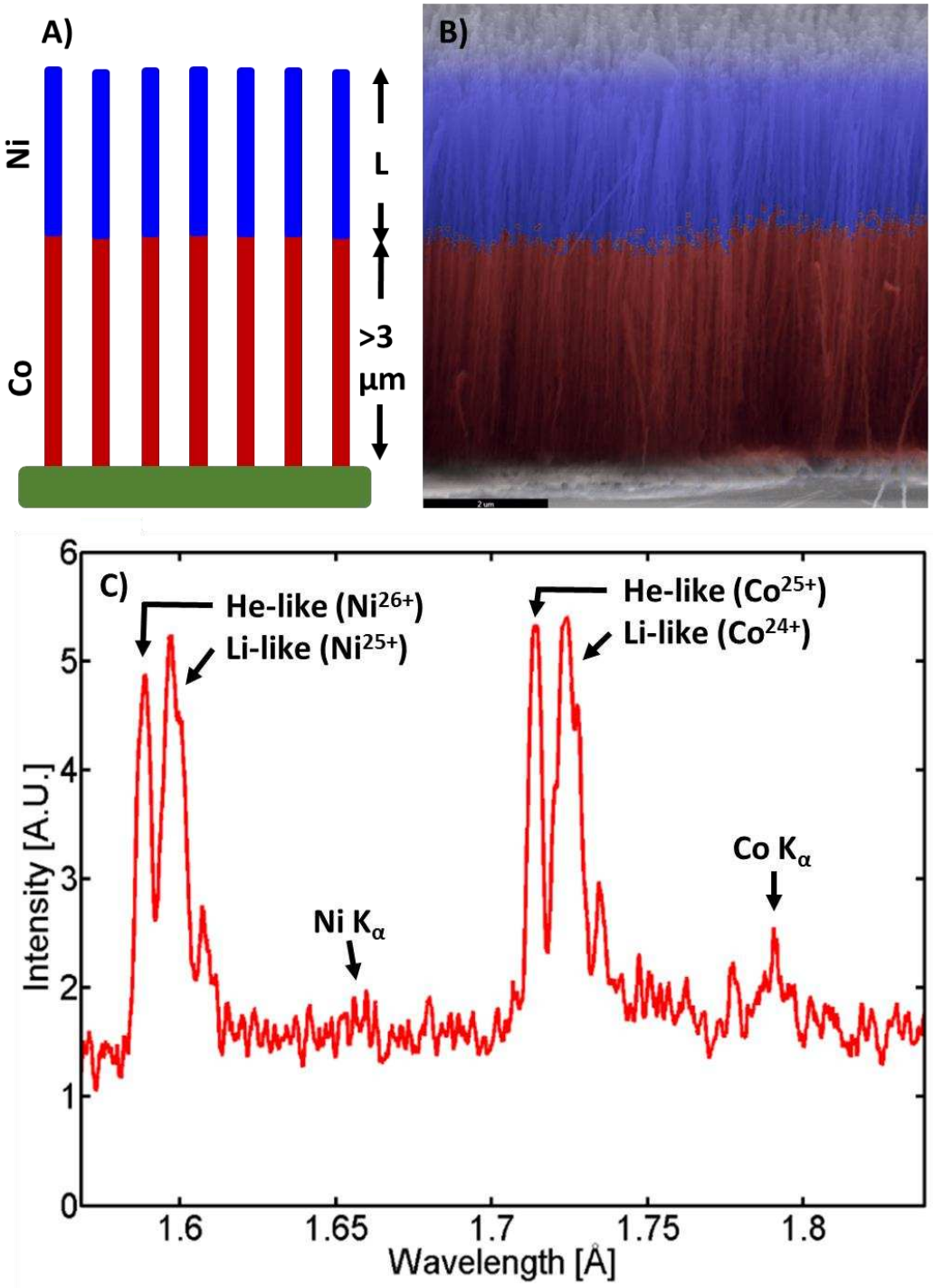

Figure 15: The compositional change along the wire length in the target arrays is depicted (A, B) along with the line spectra from each layer (C). The schematic (A) illustrates how a variable length of nickel is grown on top of a buried cobalt base that is approximately 3 µm long. An EDS image (B) shows an example of the compositional change and interface as measured for an array. Spectral lines from the two elements are observed in a single frame from the von Hamos crystal spectrometer (C).

The experiment consisted of irradiating an array of 55 nm diameter nanowires with 13% of solid density at normal incidence. The laser pulses were ultra-high contrast, frequency doubled (λ = 400 nm), 55 fs FWHM in duration, and focused on target to an intensity of up to (4 ± 1) x 10^{19} W cm^{-2}. X-ray emission from the laser-created nanowire plasma was monitored on a shot-by shot basis with the von Hamos x-ray crystal spectrometer. An approximately 3 µm long layer of cobalt nanowires acted as the buried tracer, with a variable length of nickel grown on top of this cobalt base. The example spectrum in Figure 15(c) shows lines of interest from the highly ionized Co and Ni species in the plasma produced by irradiating these two-composition nanowire arrays. Starting from the left, nickel line emission is observed for the He-α 2p-1s transition at λ = 1.588 Å, and the He-like intercombination line merged with Li-like nickel lines are found around λ = 1.597 Å. On the center right, cobalt's 2p-1s He-α transition at λ = 1.712 Å is observed next to its intercombination line, merged with Li-like cobalt near λ = 1.723 Å. The K-α lines of both species are also present, but the spectrum is dominated by line emission from highly ionized species.

Figure 16 shows spectra resulting from irradiating targets with an increasing segment length of nickel on top. Each frame is an average of 2-7 shots. The free-free Bremsstrahlung or continuum radiation is consistently present with a relative intensity of roughly one, regardless of what species dominates the spectra. Line radiation from the nickel and cobalt species that is sufficiently intense is observed above the continuum. The relative intensity of each line's radiation is dependent on its total upper level population, which in turn is determined by the volume, dependent upon the depth of the heated material. With a top layer consisting of 1.5 µm of nickel, the cobalt He-like lines clearly dominate the spectra. As the length of the top nickel layer was increased, the relative intensity of the cobalt's He-α emission from below is observed to decrease, while the intensity of the nickel lines increase accordingly.

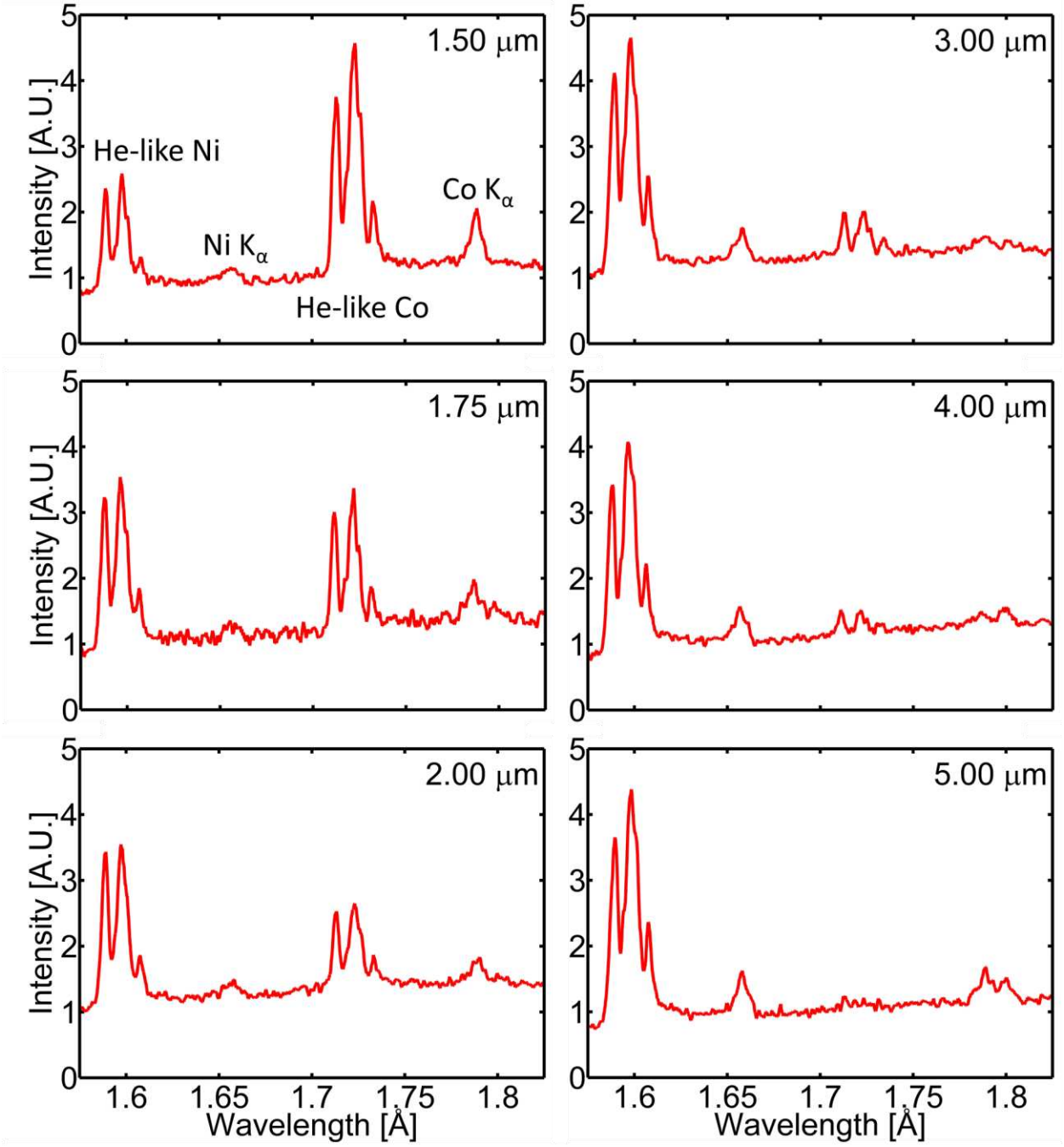

Figure 16: Series of spectra showing the variation of the intensity of the He-like nickel and cobalt lines as a function of the length of the nickel wire segment on top. The length of the top nickel wire segment (or depth of buried cobalt layer), is indicated for each spectra. These frames show that sufficient energy penetrates to a depth greater than 4 μm to ionized cobalt to its He-like state.

The measured intensity at the wavelength corresponding to the center of the He- α lines of nickel and cobalt is plotted in figure 17 as a function of buried depth. Each is well fit by an exponential. The plot shows that the buried cobalt He-α signal drops to background level at a depth between 4 and 5 µm. At this depth, there is no longer sufficient energy to ionize cobalt to its He-like state. This depth defines an energy density of over 1 x 10^9 J cm^{-3}, and definitively confirms volumetric heating of near solid-density plasma to the UHED regime. While a level of energy does penetrate deeper into the array, an in-depth discussion of the energy deposition with depth is left for the Simulations and Modeling Section.

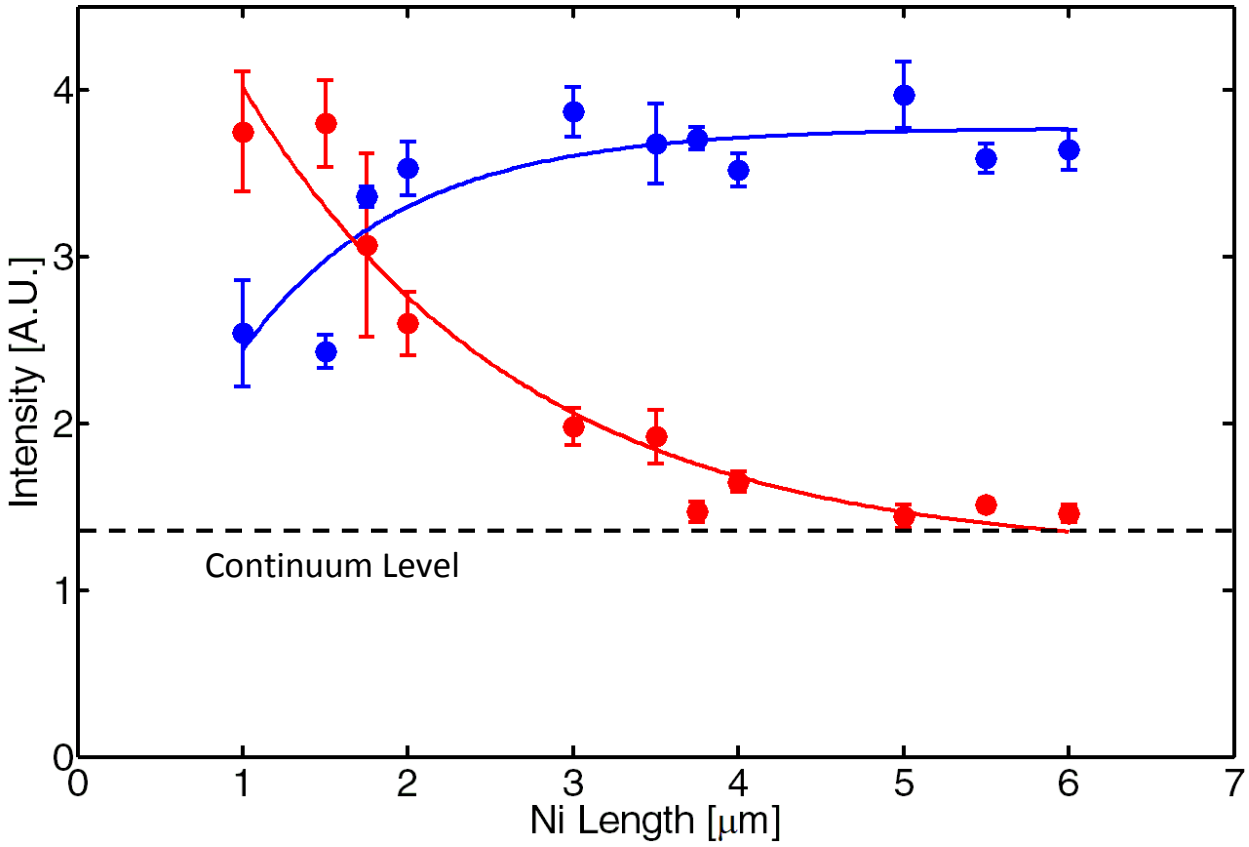

Figure 17: Intensity of the top nickel He-α (blue) and buried cobalt He-α (red) lines as a function of burying depth. Curves are well fit by exponentials. The Co line intensity nears continuum levels between 4 and 5 µm.

Section 3.2 Models and Simulations

Particle-in-Cell (PIC) and Hydrodynamic models were adapted to simulate the complex plasma dynamics underlying the observed experimental results. Modeling work was conducted by collaborators Alexander Pukhov from the Institut für Theoretische Physik, Heinrich-Heine-Universität Düsseldorf in Germany, and Vyacheslav Shlyaptsev from Colorado State University. Pukhov's relativistic Virtual Laser-Plasma Laboratory (VLPL) code [1] was used with the capabilities of its standard algorithm extended by packages for optical-field ionization (OFI), binary collisions, and electron impact ionization. OFI was treated as an under-barrier tunneling phenomenon in the static electric field [2, 3] with only sequential field ionization considered. The probabilities for Coulomb collisions between all particles in one mesh cell were calculated by the Binary Collision Package.

PIC simulations utilized a three-dimensional geometry, and self-consistently included ionization physics for both Ni and Co atomic species present in the target. The simulated nanowire arrays were composed of 55 nm diameter wires with an upper nickel segment and lower cobalt segment, arranged with a 135 nm periodicity corresponding to an array with density 13% of solid. A linearly polarized plane wave with 400 nm wavelength and Gaussian time-envelope $a(t) = a_0 \exp(-t^2/\tau^2)$ was used to simulate the laser pulse where the relativistic amplitude $a_0 = eA/mc^2 = 2.16$ corresponds to a laser intensity of $I_0 = 4 \times 10^{19}\ W/cm^2$ and a 55 fs FWHM pulse duration. The laser pulse was made to impinge on the nanowire array at normal incidence. The PIC simulation space consisted of a cell volume encompassing the wires and inter-wire gaps, as well as space above the array to allow for expansion of the wire material as it explodes and thermalizes. The simulation describes all phases of the laser's interaction with the nanowire array and subsequent explosion and thermalization. The code accounts for local field enhancements [4],

field fluctuations, and resonance heating [5]. Bulk resonances, however, will not be present due to the average density being higher than the critical density and the spacing of the nanowires being smaller than the wavelength of the laser.

PIC results showing the evolution of the plasma at four different time points after the peak of the laser pulse reaches an array with 1.5 µm of Ni on top of a 4.0 µm Co base can be seen in Figure 18. OFI begins the heating process at the boundary of the nanowire array as the strong electric field of the laser pulse strips electrons, creating ionization states up to Z = 18. Collisional electron impact ionization produces higher ionization states as the hot electron population heats deep into the nanowire cores. A high average density surpassing 10^{24} cm^{-3} with peak pressures of nearly 200 Gbar is quickly reached inside the wires near their tips (+4 fs frame in Figure 18). The laser pulse can continue to propagate down the length of the wires and deep into the array as long as the inter-wire gaps remain free from dense plasma. In the two earliest frames (+4 fs and +44 fs frames in Figure 18), the wire tips appear to be loosely connected by lines of warmer color, indicating an inter-wire region of higher energy density. This is a result of the square array geometry. The inter-wire gaps are narrower directly between wires along the square edges than across the diagonal. These narrower gap regions thus fill with particles quicker and reach higher energy densities faster than the diagonal regions. Expansion of the wire continues to close all inter-wire gaps along the length of the wires (+124 fs frame in Figure 18) until the high energy density of the wire cores is fully transformed into a thermal energy density of nearly 1 GJ cm^{-3} along the length of the wire array (+304 fs frame in Figure 18). A thermalized electron temperature of 10 - 20 keV is reached over the plasma volume, with an average density of over 3 x 10^{23} cm^{-3}.

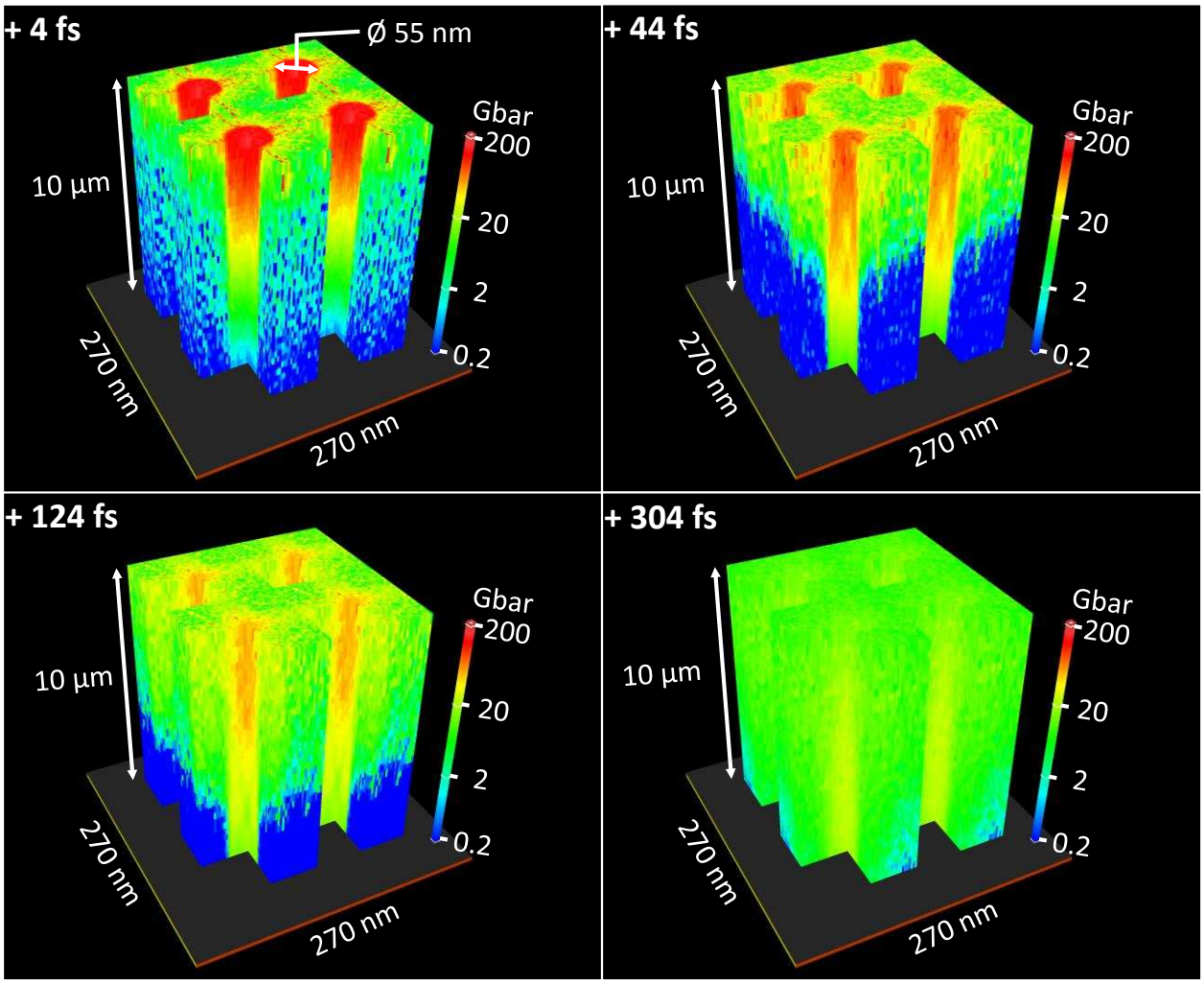

Figure 18: PIC simulation of a femtosecond laser pulse of relativistic intensity irradiating an array of vertically aligned nanowires. Each frame corresponds to a different time point, indicated in the top-left corner of each frame, after the peak of the laser pulse has reached the top boundary of the array. The array consists of nanowires 55 nm in diameter with a 135 nm periodicity. The top 1.5 µm of each wire in the array is composed of Ni atoms, while the remainder is composed of Co atoms. The laser pulse comes from the top, impinging on the array at normal incidence. Relativistic laser pulses are modeled by plane waves with an intensity of 4 x 10^{19} W cm^{-2}, λ = 400 nm wavelength, and 55 fs FWHM temporal duration.

Once enough time has passed for the plasma to thermalize, more computationally efficient hydrodynamic codes can be used to model subsequent plasma dynamics, including ionization states over the plasma volume. Modeled radiation spectra emitted by the plasma was generated by post-processing the VLPL output based on the time and space history of electron and ion distribution functions. Cross sections from the atomic code HULLAC [6] were integrated with these distribution functions to get the atomic process rates. Atomic kinetics and radiation transport were then calculated using the RADEX [7] code. These rates were also used to model spectral linewidths as collisional broadening is the dominant broadening process in such dense plasma.

The (Co He-α)/(Ni He-α) line intensity ratio from radiation emitted by the plasma was calculated and compared with experimental values in Figure 19. The ratio was calculated for only three lengths of the top Ni layer due to the cost of running such complex codes. Simulated ratios for these three lengths agree remarkably well with experimental values, and fall very nearly on the exponential line of best fit to the experimental values. It can be seen that as the length of the top nickel segment reaches 5 μm in length, the ratio approaches the labeled "continuum level" line. This level represents a saturation of the nickel He-like lines and a simultaneous disappearance of the cobalt He-like lines as they become indistinguishable from the background level. A simulated spectra over the experimentally observed 1.55 – 1.85 Å region was synthesized, and can be seen as the inset of Figure 19. Again, this agrees remarkably well with the experimentally observed spectra from Figure 16, replicating all of the key spectral features, including satellite and intercombination lines.

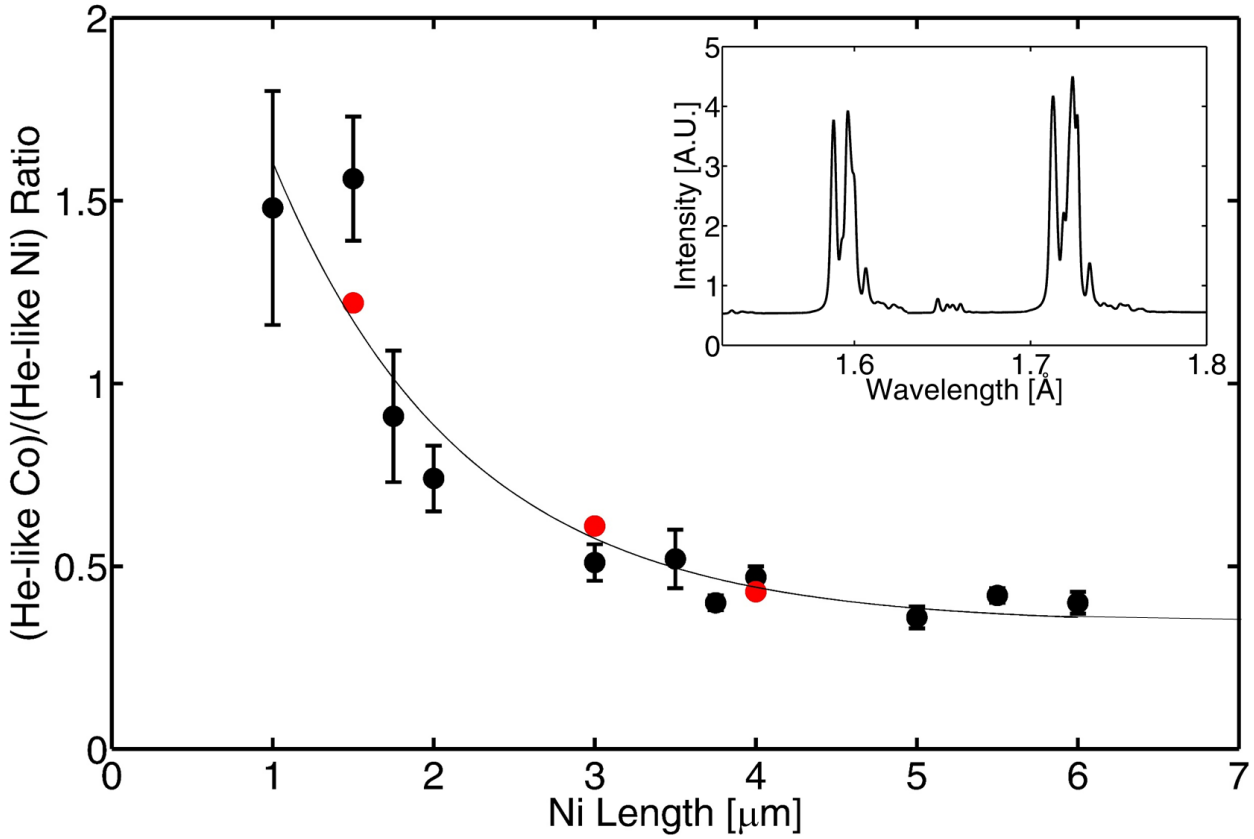

Figure 19: Experimental and simulated (Co He-α)/(Ni He-α) ratios are compared in the main plot while a synthetic spectra for an array with a 1.5 μm long top Ni layer is shown in the insert. The simulated ratios (red dots) very nearly match the exponential line of best fit (solid line) to the experimental data (black dots). The synthetic spectra also closely replicates the observed features of the experimental data as seen in Figure 16. The Co He-like signal can no longer be distinguished from background at the continuum level, reached with a 4-5 μm long top Ni layer.

Section 3.3 Conclusions

Nanowire arrays have proven to be excellent targets for trapping laser pulses of relativistic intensity deep inside the material, allowing for the volumetric creation of UHED plasma. Inter-wire gaps keep the average target density high, near that of solid, but overcome the limitation of the critical density surface. High degrees of ionization were observed in arrays composed of nickel and cobalt, with the He-like lines dominating that of K-α, a phenomena which only occurs in a hot

dense plasma. Experimental results from buried tracer experiments show the presence of He-like cobalt ions to depths greater than 4 μm when arrays with density 13% of solid and 55 nm diameter wires are irradiated by ultrahigh contrast femtosecond pulses at an intensity of $(4 \pm 1) \times 10^{19}$ W cm^{-2}. PIC and hydrodynamic simulations reproduce the experimental results with good accuracy and compute the plasma parameters to be exceptional. Tips of the wire cores are calculated to initially reach nearly 200 Gbar pressures. After the wires explode and thermalize, a thermal energy density of nearly 1 GJ cm^{-3} is reached along the wire length, nearly two orders of magnitude larger than that found in the plasma in an inertial confinement fusion hohlraum [8, 9]. This is comparable to the central hot-spots created using ultra-high laser energies at the National Ignition Facility (NIF), and only surpassed when the NIF capsule is highly compressed [9].

The fact that this extreme state of matter has been created with a compact table-top laser system that is far more widely reproducible and cost effective than the large national facilities is one of the projects greatest achievements. For the first time, such extreme conditions have been made accessible in a manner that allows for wide-spread study and application. While these experiments were conducted using modest laser energies of ~ 0.6 J, our simulations predict that irradiating the vertically aligned nanowire arrays with higher energy pulses will lead to the creation of plasma with unprecedented degrees of ionization for dense laboratory plasmas. For example, codes predict that irradiating uranium nanowire arrays with laser intensities greater than 1×10^{20} W cm^{-2} will create thermalized plasma densities in excess of 1×10^{24} cm^{-3} and dominated by atoms that are more than 70 times ionized. Increasing the laser irradiation intensity to 1×10^{22} W cm^{-2} is predicted to result in pressures larger than those in the center of the sun. These are plasma conditions of great interest for future investigations.

REFERENCES

1. A. Pukhov, *Three-dimensional electromagnetic relativistic particle-in-cell code VLPL (Virtual Laser Plasma Lab)*. Journal of Plasma Physics, 61, 425-433 (1999).
2. A. Zhidkov, A. Sasaki, *Effect of field ionization on interaction of an intense subpicosecond laser pulse with foils*. Physics of Plasmas, 7, 1341-1344 (2000).
3. A. Karmakar, A. Pukhov, *Collimated attosecond GeV electron bunches from ionization of high-Z material by radially polarized ultra-relativistic laser pulses*. Laser and Particle Beams, 25, 371-377 (2007).
4. S. Mondal, et al., *Highly enhanced hard x-ray emission from oriented metal nanorod arrays excited by intense femtosecond laser pulses*. Phys. Rev. B, 83, 035408 (2011).
5. F. Brunel, *Not-so-resonant, resonant absorption.* Phys. Rev. Lett., 59, 52-55 (1987).
6. M. Klapisch, et al., *A New and Improved Version of HULLAC*. AIP Conf. Proc. 926, 206 (2007).
7. V. N. Shlyaptsev, et al., *Dynamics of a Capillary Discharge Soft X-ray Laser,* Proc. SPIE Int. Soc. Opt. Eng. 2520, 365 (1995).
8. MacGowan B.J. et al. *Laser-plasma interactions in ignition scale hohlraum plasmas*. Phys. Plasmas. **3**, 2029-2040 (1996).
9. S. Le Pape, et al., *Observation of a reflected shock in an indirectly driven spherical implosion at the National Ignition Facility*. Phys. Rev. Lett. 112, 1 (2014).